Type-II Dirac line node in strained Na_3N

Dongwook Kim,[1] Seongjin Ahn,[2] Jong Hyun Jung,[2] Hongki Min,[2] Jisoon Ihm,[3] Jung Hoon Han,[1] and Youngkuk Kim[1,*]

[1]*Department of Physics, Sungkyunkwan University, Suwon 16419, Korea*

[2]*Department of Physics and Astronomy, Seoul National University, Seoul 08826, South Korea*

[3]*Department of Physics, Pohang University of Science and Technology, Pohang 37673, South Korea*

(Received 23 July 2018; revised manuscript received 12 September 2018; published 11 October 2018)

Dirac line node (DLN) semimetals are a class of topological semimetals that feature band-crossing lines in momentum space. We study the type-I and type-II classification of DLN semimetals by developing a criterion that determines the type using band velocities. Using first-principles calculations, we also predict that Na_3N under an epitaxial tensile strain realizes a type-II DLN semimetal with vanishing spin-orbit coupling, characterized by the Berry phase, which is $\mathbb{Z}_2$ quantized in the presence of inversion and time-reversal symmetries. The surface energy spectrum is calculated to demonstrate the topological phase and the type-II nature is demonstrated by calculating the band velocities. We also develop a tight-binding model and a low-energy effective Hamiltonian that describe the low-energy electronic structure of strained Na_3N. The occurrence of a DLN in Na_3N under strain is captured in the optical conductivity, which we propose as a means to experimentally confirm the type-II class of DLN semimetals.

DOI: 10.1103/PhysRevMaterials.2.104203

I. INTRODUCTION

During the past decade, topological semimetals have been an active subject of condensed matter physics and quantum materials, providing a unique venue for exotic phenomena originating from band topology [1–4]. Since the discovery of Weyl semimetals [5–17], various classes of topological semimetals have been found theoretically and experimentally, including Dirac semimetals [18–26], nodal line semimetals [5,25–48], and their diverse variations such as multi-Weyl semimetals and double-Dirac semimetals [49–53].

More recently, the classification of topological semimetals is further specified into the type-I and type-II classes based on the geometric structure of the Fermi surface [53–60]. The type-I material features a closed Fermi surface enclosing the nodes; in contrast, type-II material features an open Fermi surface composed of electron and hole pockets that linearly touch at the nodes. First proposed in Weyl semimetals, the type-I/II classification has been extended to Dirac semimetals [53,58,61–64] and nodal line semimetals [65–67]. In the case of Weyl semimetals, this classification provides an important insight for understanding unique phenomena present only in type-II materials, such as the squeezing or collapse of Landau levels, Klein tunneling, and magnetic breakdown in momentum space when magnetic fields are applied to overtilted Weyl nodes [68–71]. Some papers have already proposed type-II Dirac line nodes (DLNs) and reported relevant materials hosting such kinds of DLNs [65–67]. Contrasting features of type-I and type-II DLNs have been identified in terms of their dispersion and Fermi surface geometry [65].

In this paper we go beyond the well-known characterization of type-II DLNs and identify a more fundamental way to understand and identify the type-II class of DLN semimetals. Based on geometric argument, a concrete connection is established between the sign inversion of band velocities around a type-II DLN and the occurrence of open Fermi surface in type-II DLN semimetals, which leads to a rigorous criterion to determine the types of DLNs. We use this criterion and first-principles calculations to predict that epitaxially strained Na_3N realizes a type-II DLN semimetal phase. The nontrivial band topology and type-II nature of the DLN semimetal are explored. We also construct a tight-binding model and a low-energy effective theory and use them to rationalize the low-energy electronic structure and to calculate the optical conductivity of Na_3N. The optical response significantly changes upon straining due to the occurrence of a type-II DLN semimetal, which can be experimental evidence of the type-II DLN semimetal phase hosted in strained Na_3N.

This paper is structured as follows. First, we begin with the background in Sec. II, which provides simple and intuitive ways to understand the type-I versus type-II nature of DLNs. Following that, we contrast in Sec. III the electronic band structures of pristine and strained Na_3N. This clarifies the electronic structure of Na_3N, which is responsible for the occurrence of a DLN under strain. Next, in Sec. IV, topological characterization of strained Na_3N is discussed in terms of the $\mathbb{Z}_2$ topological indices and surface energy spectrum. Also, the type-II nature is demonstrated via the band velocities evaluated in the vicinity of the DLN. Then, in Sec. V, we construct a tight-binding model for Na_3N, reproducing the main features of the density functional theory (DFT) calculations. Physical manifestations of the type-II DLN nature are predicted to occur as unique features in the surface spectrum and the optical conductivity, as demonstrated in Sec. VI. Finally, we conclude the paper with a summary and perspective in Sec. VII.

*youngkuk@skku.edu

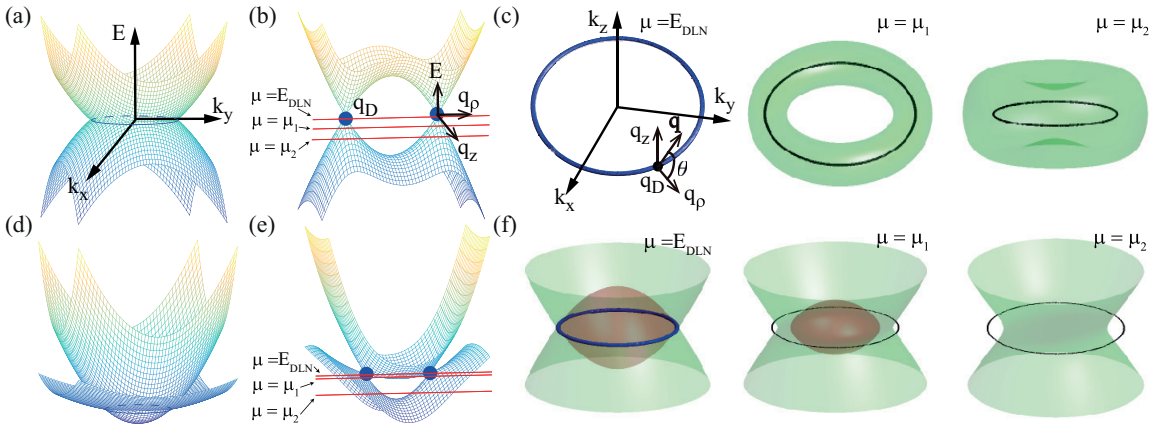

FIG. 1. Typical energy band dispersions and Fermi surfaces of type-I (first row) and type-II (second row) DLNs. (a), (b) Electronic energy bands of a type-I DLN on the k_x-k_y and k_ρ-k_z planes, respectively. Here $k_\rho = \sqrt{k_x^2 + k_y^2}$ and the DLN lies on the k_x-k_y plane. (c) Changes in the Fermi surface for a type-I DLN in 3D momentum space as the chemical potential is tuned from $\mu = E_{\rm DLN}$, μ_1 to μ_2. The locations of $E_{\rm DLN}$, μ_1, and μ_2 in energy are shown in (b). Blue circles in (c) indicate the position of the DLN. Green surfaces represent the Fermi surface at the corresponding chemical potentials. $\boldsymbol{q} = \boldsymbol{k} - \boldsymbol{k}_{\rm D}$ is the relative momentum defined with respect to a point in the DLN at $\boldsymbol{k}_{\rm D}$. The left panel in (c) defines the in-plane q_ρ and out-of-plane q_z components of the relative momentum $\boldsymbol{q}$. (d), (e) Typical energy bands of a type-II DLN on the k_x-k_y and k_ρ-k_z planes. (f) Corresponding changes in the Fermi surface for a type-II DLN at $\mu = E_{\rm DLN}$, μ_1, and μ_2. Blue circles in (f) indicate the position of the DLN. Green (red) surfaces represent electron (hole) pockets. At $\mu = E_{\rm DLN}$, the DLN coexists with the electron and hole pockets that touch each other linearly at the DLN.

II. BACKGROUND

We start with a brief review of the mathematical foundation for type-II DLN semimetals. Similarly to the Weyl semimetal case [54], distinguishing aspects of type-II DLNs lie in their dispersion and the Fermi surface geometry: the existence of an overtilted Dirac cone and an open (or extended) Fermi surface [65]. Figures 1(a) and 1(d) illustrate the contrasting shape of energy bands of type-I and type-II DLNs on the k_x-k_y plane where the line node lies. Also, Figs. 1(b) and 1(e) show contrasting energy bands of type-I and type-II DLNs featured on the k_ρ-k_z plane for a fixed value of in-plane angle $\tan^{-1}(k_y/k_x)$, where $k_\rho = \sqrt{k_x^2 + k_y^2}$ is the radial momentum. The k_ρ-k_z plane intersects with the DLN at two points on the DLN. The intersecting points of the DLN and the k_ρ-k_z plane are indicated by blue dots in Figs. 1(b) and 1(e). These intersecting points appear as Dirac points with linear dispersions away from the points on this normal plane. Hereafter, we refer to them as Dirac points.

While the energy dispersions are linear in both type-I and type-II DLNs in the vicinity of the nodal line, the difference between them is clear in the band velocities at the DLN. Recall that two independent directions exist in moving away from a given point on the DLN, which define a plane locally normal to the tangent direction of the DLN. If the band velocities are opposite for the conduction and the valence bands regardless of the direction away from the Dirac point in this normal plane, we refer to this as a *conventional* type-I DLN. In contrast, if the band velocities of the conduction and valence band have the same sign for some direction away from the DLN in the normal plane, we refer to it as an *unconventional* type-II DLN. These different types give rise to the second distinguishing characteristic, manifested in the Fermi surface geometry. As illustrated in Figs. 1(c) and 1(f), as one varies the chemical potential μ [red lines in Figs. 1(b) and 1(e)], the hole (electron) pocket appears as a green (red) surface. Irrespective of the chemical potential μ, the Fermi surface (equally, constant energy surface at $E = \mu$) of a type-I (type-II) DLN exists in a closed (open) surface, in line with the previous study in [65].

Instead of inspecting the band velocities, the classification is also possible by the Fermi surface geometry, similarly to the case of Weyl points [54]. To specify this, we first introduce two coordinate systems used in the discussion throughout the paper. The first one is the $\boldsymbol{k} = (k_x, k_y, k_z)$ coordinates in the Brillouin zone (BZ) describing the global structure of a DLN. The second set of coordinates is a relative coordinate system $\boldsymbol{q} = (q_x, q_y, q_z)$ with the origin at a Dirac point of the DLN $\boldsymbol{k}_{\rm D}$ [Fig. 1(c)], which describes the local behavior of the energy bands. The two coordinate systems are related by $\boldsymbol{k} = \boldsymbol{k}_D + \boldsymbol{q}$, where $\boldsymbol{k}_D$ refers to a point on the DLN.

In general, the nodal structure of two bands can be described by the 2×2 Hamiltonian

$$H = \sum_{j=1}^{3} d(\boldsymbol{q})_j \sigma_j, \tag{1}$$

with the Pauli matrices σ_j's. When the Hamiltonian is linear in $\boldsymbol{q}$, one can find a linear map $\boldsymbol{A} : V \to W$ from $\boldsymbol{q}$ to $\boldsymbol{d}$, where $\boldsymbol{q} \in V$, $\boldsymbol{d} \in W$, and

$$H = \sum_{j=1}^{3} d_j \sigma_j = \sum_{i,j=1}^{3} q_i A_{ij} \sigma_j. \tag{2}$$

Band-gap closing points generically occur at $\boldsymbol{q}$ points that satisfy $d_j(\boldsymbol{q}) = 0$ for all j's. Depending on the dimensions of the null space (or kernel space) of the linear map $\boldsymbol{A}$, which can be either zero, one, or two, the gap closing points constitute

points, lines, or planes, respectively. The kernel dimensions determine the dimensions of the quotient space $V/\ker\mathbf{A}$ and also the dimensions of the image space of the linear mapping $\mathrm{im}\mathbf{A}$ as $\mathrm{Dim}(V) - \mathrm{Dim}(\ker\mathbf{A})$. We can rewrite the low-energy Hamiltonian using the new linear mapping $\tilde{\mathbf{A}}$ from $V/\ker\mathbf{A}$ to $\mathrm{im}\mathbf{A}$ with reduced dimensions ($\tilde{\mathbf{A}} : V/\ker\mathbf{A} \to \mathrm{im}\mathbf{A}$, $\boldsymbol{k} \in V/\ker\mathbf{A}$, and $\boldsymbol{d} \in \mathrm{im}\mathbf{A}$). Now this new linear mapping describes only the linear dispersion in the two directions that are locally orthogonal to the nodal line direction. As a result, in the case of nodal line [$\mathrm{Dim}\ \ker\mathbf{A} = 1$], the local behavior of electrons is described by the low-energy Hamiltonian with the reduced dimensions [$\mathrm{Dim}\ V/\ker\mathbf{A} = 2$]:

$$H = \sum_{i,j=1}^{2} q_i \tilde{A}_{ij} \sigma_j + \sum_{i=1}^{2} w_i q_i. \tag{3}$$

Here "local" means that the wave vector $\boldsymbol{q}$ is expanded from a particular point on the nodal line [see Fig. 1(c)]. Representing the position of a point constituting the DLN as $\boldsymbol{k}_D$, wave vectors in the BZ are expanded up to the linear order $\boldsymbol{q} = \boldsymbol{k} - \boldsymbol{k}_D$, leading to the low-energy Hamiltonian, Eq. (3), that describes a Dirac cone in two dimensions. The second term in the Hamiltonian is introduced to describe the tilting of the Dirac cones, which plays a crucial role in enabling type-II DLNs. As in the case of the Weyl point [54], the Fermi surface equation, which is a conic section equation in the DLN case, gives either an open or a closed solution, which defines the type-I/type-II classifications.

In detail, two energy eigenvalues are obtained from Eq. (3) as

$$E_{\pm} = \sum_{i=1}^{2} w_i q_i \pm \sqrt{\sum_{i,j=1}^{2} q_i [\tilde{A}\tilde{A}^T]_{ij} q_j}. \tag{4}$$

The Fermi surface equation that satisfies $E_{\pm} = \mu$ is obtained as

$$\sum_{i=1}^{2} q_i (w_i w_j - [\tilde{A}\tilde{A}^T]_{ij}) q_j - 2\mu \sum_{i=1}^{2} w_i q_i + \mu^2 = 0. \tag{5}$$

When $\det(\boldsymbol{w} \otimes \boldsymbol{w} - [\tilde{A}\tilde{A}^T]) > 0$ [$\det(\boldsymbol{w} \otimes \boldsymbol{w} - [\tilde{A}\tilde{A}^T]) < 0$], Eq. (5) describes a conic section equation that gives an elliptic [a hyperbolic] curve. Thus, DLNs are classified into two types: type-I for the elliptic (closed) curve and type-II for the parabolic (open) curve. It is noteworthy that, in general, the tilting coefficient $\boldsymbol{w}$ can be a function of $\boldsymbol{k}$, although it is treated as a constant for simplicity in the above derivation. When the tilting coefficient varies, such that $\det(\boldsymbol{w} \otimes \boldsymbol{w} - [\tilde{A}\tilde{A}^T])$ changes the sign along the DLN, which can happen in highly anisotropic systems that reside near the transition between this type-I and type-II, the sign change of the determinant identifies a novel-type hybrid DLN [72]. While this case shares the characteristic features of type-II DLNs hosting the electron and hole pockets that coexist with the DLN, it also allows for diverse possibilities in the Fermi surface geometry, which could be of particular interest with respect to quantum oscillations and transport phenomena.

Another way of sorting out the types of DLNs is by looking at the sign inversion of band velocities. Since the matrix $\tilde{\mathbf{A}}\tilde{A}^T$ is Hermitian with nonnegative eigenvalues $\lambda_1^2, \lambda_2^2 > 0$ (we assume the generic situation of nonzero eigenvalues), the energy dispersion after the rotation to the principal axis becomes

$$E_{\pm} = w_1 q_1 + w_2 q_2 \pm \sqrt{(\lambda_1 q_1)^2 + (\lambda_2 q_2)^2}. \tag{6}$$

After rescaling the variables $q_1 \to q_1/\lambda_1$, $q_2 \to q_2/\lambda_2$ and introducing the polar coordinates $\boldsymbol{q} = (q_1, q_2) = q(\cos\theta_q, \sin\theta_q)$, one can further simplify the energy equation [Eq. (6)] to

$$\begin{aligned} E_{\pm} &= \pm v_{\pm} q, \\ v_{\pm} &= 1 \pm \sqrt{\frac{w_1^2}{\lambda_1^2} + \frac{w_2^2}{\lambda_2^2}} \cos[\theta_{\boldsymbol{q}}]. \end{aligned} \tag{7}$$

Here, $\theta_{\boldsymbol{q}}$ measures the angle from one of the principal axes. The conventional type-I Dirac cone shown in Fig. 1(b) is realized if the radial velocity satisfies $v_+ v_- > 0$ for all orientations $\theta_{\boldsymbol{q}}$ or, equivalently, when

$$1 - \sqrt{\frac{w_1^2}{\lambda_1^2} + \frac{w_2^2}{\lambda_2^2}} > 0. \tag{8}$$

Otherwise, the unconventional type-II Dirac cone shown in Fig. 1(e) is realized with $v_+ v_- < 0$ over some range of $\theta_{\boldsymbol{q}}$. After some unraveling of the algebra, one can prove that Eq. (8) is equivalent to the condition $\det(\boldsymbol{w} \otimes \boldsymbol{w} - [\tilde{A}\tilde{A}^T]) > 0$. This proves that the classification scheme in terms of the conic section is equivalent to the scheme in terms of the sign inversion of the band velocity.

The difference in the type-I and type-II band structures can be understood in the language of differential geometry as well. The band velocities along the principal axes are the well-known principal curvatures in differential geometry, and their product is the Gaussian curvature that indicates the shape of the surface. For either the conduction band or the valence band [$E_{\pm}$ in Eq. (7)], coordinates along the principal axes are (q_1, q_2) and the corresponding velocities (or principal curvatures) are given by $v_{\pm,1(2)} = \partial E_{\pm}/\partial q_{1(2)}$, respectively. The Gaussian curvatures for each band follow from $K_{\pm} = v_{\pm,1} v_{\pm,2}$. In type-I (type-II) DLNs, the product of Gaussian curvatures

$$K_+ K_- = v_{+,1} v_{+,2} v_{-,1} v_{-,2} = 1 - \left(\frac{\omega_1^2}{\lambda_1} + \frac{\omega^2}{\lambda_2^2}\right) \tag{9}$$

is positive (negative). The final expression on the right follows from Eq. (8). As a result, all three methods, i.e., conic section classification, sign inversion of the band velocity, and band curvature analysis, yield the same conclusion with regard to the type-I/II classification of DLNs. In the type-II DLN, either the conduction band or the valence band has a saddle-shaped band structure in the (q_1, q_2) space.

III. METHODS AND ELECTRONIC BAND STRUCTURE

A. Calculation methods

Having identified the physical and mathematical conditions to distinguish type-I and type-II DLNs, we now show that

Na_3N under strain realizes a type-II DLN. Before showing the first-principles results, we list the details of computational methods. Our first-principles calculations are based on density functional theory in the Perdew-Zunger-type local density approximation (LDA) [73]. The norm-conserving, optimized, designed nonlocal pseudopotentials are generated using OPIUM [74]. The wave functions are expanded in the plane-wave basis as implemented in the QUANTUM ESPRESSO package [75]. The energy cutoff for the basis is set to 680 eV. The atomic structure is fully relaxed within the force threshold of 0.005 eV/Å and the $8 \times 8 \times 8$ Monkhorst-Pack grid [76] is used for k-point sampling. The surface spectra are obtained by calculating the surface Green's function for a semi-infinite geometry [77,78], using the Wannier Hamiltonian, generated using WANNIER90 [79–82]. For Wannierization, the conduction and valence states are initially projected to the s orbitals of K and Na and the p orbitals of N. The lattice constant of Na_3N is calculated as $a = 4.67$ Å. The lattice constant of strained Na_3N is calculated by fixing a and relaxing the other lattice parameter. In the case of 5% tensile strain, we fixed a to 4.91 Å and relaxed c, resulting in 4.63 Å. The Poisson ratio for the epitaxial strain is calculated as 0.2. In order to show the robustness of our LDA results, the hybrid functional calculation for the electronic band structure is performed using VASP [83], employing the Heyd-Scuseria-Ernzerhof (HSE06) scheme for the exchange-correlation potential [84]. Although spin-orbit coupling (SOC) is negligibly weak in Na_3N, the effect of SOC is considered in Appendix B for the sake of completeness of the study by using full-relativistic pseudopotentials based on noncollinear spin calculations.

B. Crystal structure and symmetries

Figure 2(a) illustrates the primitive unit cell of Na_3N in the anti-ReO_3 structure, which comprises one N atom at the corner and three Na atoms at the center of each edge. The crystalline symmetries belong to the cubic space group $Pm\bar{3}m$ (No. 221), generated by inversion and three rotations. Under the epitaxial strain shown in Fig. 2(b), the cubic crystalline symmetry is broken into the $P4/mmm$ (No. 123) tetragonal space-group symmetry. The $P4/mmm$ space group is generated by inversion $\mathcal{P}$, reflection $\mathcal{M}_x$, and fourold rotation C_{4z}. Together with these crystalline symmetries, time-reversal symmetry $\mathcal{T} = \mathcal{K}$ plays the important role of providing topological protection of the DLN. Here $\mathcal{K}$ is the complex conjugation operator. Figures 2(c) and 2(d) show the BZ of pristine Na_3N and strained Na_3N, respectively. We find that the Γ point in pristine Na_3N hosts a triply degenerate state (not counting the spin degeneracy), which evolves into a DLN encircling Γ lying on the $k_z = 0$ plane under the strain. The evolution of the triply degenerate point to a DLN is detailed in Sec. IV A.

C. Electronic band structure

Figures 3(a) and 3(b) show the electronic band structures of pristine and 5% epitaxially tensile strained Na_3N obtained from our first-principles calculations without SOC. It is clear that the band structures of both cases are semimetallic, with the electron and hole pockets forming near the Γ and M

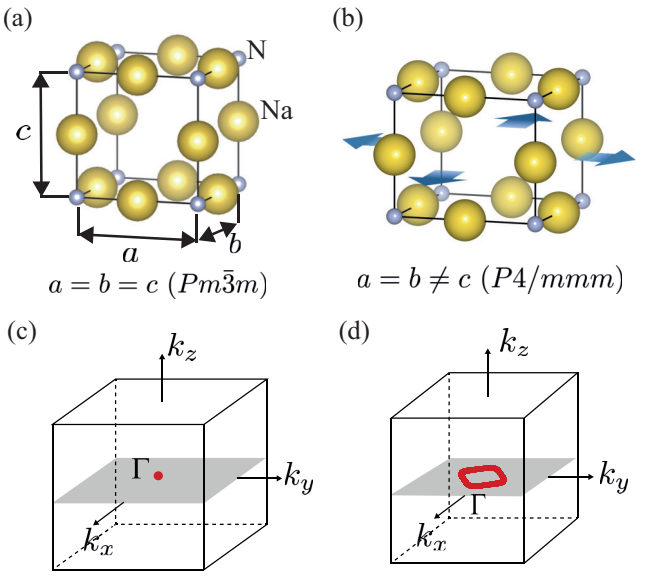

FIG. 2. Atomic structures of (a) pristine and (b) strained Na_3N. Blue arrows illustrate the direction of strain, which lowers the cubic $Pm\bar{3}m$ space-group symmetry to the tetragonal $P4/mmm$ space-group symmetry. Brillouin zones of (c) pristine Na_3N and (d) strained Na_3N. A nodal point in pristine Na_3N and a DLN of strained Na_3N are shown in red.

points, respectively. The electronic energy states in the energy range presented in Figs. 3(a) and 3(b) are mainly composed of the Na s and N p orbitals, and the contribution from the N s orbital is negligible. In the pristine case, at Γ, we find that the valence-band top and the conduction-band bottom are fused to form a triply degenerate T_{1u} state right below the Fermi energy, comprising the N p_x, p_y, and p_z orbitals, indicated by the red circle in the inset in Fig. 3(a). In addition, a single A_{1g} state resides 0.67 eV below the T_{1u} state at Γ, which is built out of the Na s orbitals. An epitaxial strain gives rise to a tetragonal crystal field, which splits the triply degenerate T_{1u} state into a doubly degenerate E_u state and a single A_{2u} state. Tensile (compressive) strain raises (lowers) the energy of the A_{2u} state with respect to the doubly degenerate E_u state at Γ. As the strain increases, the energy splitting between the E_u and the A_{2u} states becomes larger. The energy raising of A_{2u} under a tensile strain enables crossing between A_{2u} and A_{1g} bands. Notably, crossing does not happen when applying a compressive strain that lowers the energy of the A_{2u} state. The inversion of the A_{1g} and A_{2u} states is responsible for the occurrence of a DLN in strained Na_3N, which occurs along the high-symmetry line Γ-M or Γ-X. This results in band-crossing points indicated by the red circles in Figs. 3(b) and 3(c).

As it is well known that the LDA tends to underestimate the band gap (or, equally, overestimate the band inversion), we also calculated the HSE06 band structure and found that the semimetallic feature is reproduced [85]. Nonetheless, it is worth mentioning that, depending on the exchange-correlation functionals, the band structure of Na_3N could be semiconducting. Indeed, some literature [86,87] claims that Na_3N is a semiconductor when a different exchange-correlation energy functional is used. We discuss this further in Sec. VII. We

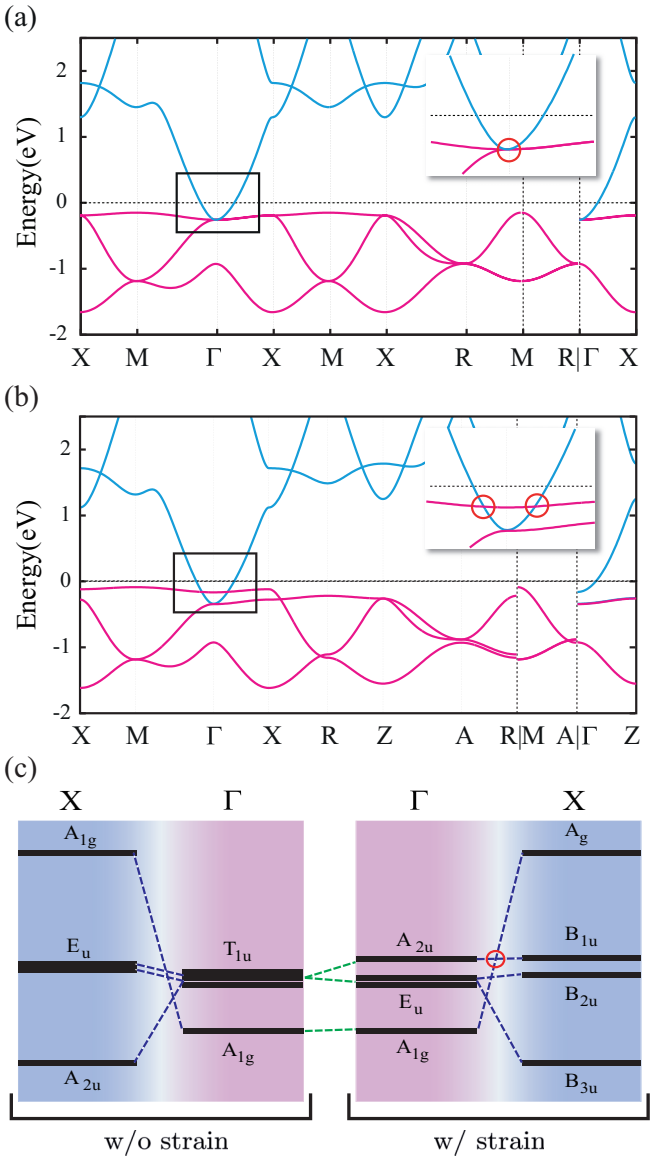

FIG. 3. Electronic band structures of (a) pristine and (b) 5% strained Na_3N. Band structures are drawn along high-symmetry lines in the BZs of cubic and tetragonal unit cells, respectively. Conduction (valence) bands are represented by blue (red) lines. The triply degenerate point in Na_3N and doubly degenerate points in strained Na_3N are indicated by red circles. (c) Diagram showing the evolution of energy ordering from Γ to X for pristine Na_3N and strained Na_3N. Lifting of triple degeneracy leads to the formation of a DLN.

point out that the remainder of the discussion is based on our LDA and HSE06 results.

IV. TYPE-II DLN IN STRAINED Na_3N

As illustrated in Fig. 2(d), an epitaxial tensile strain applied to Na_3N engenders a DLN of the type-II class. In this section, we first show that strained Na_3N hosts a DLN in momentum space. The crossing points that we found off the high-symmetry Γ point in the band structure indicate the presence of a DLN. From this indication, we identify the states

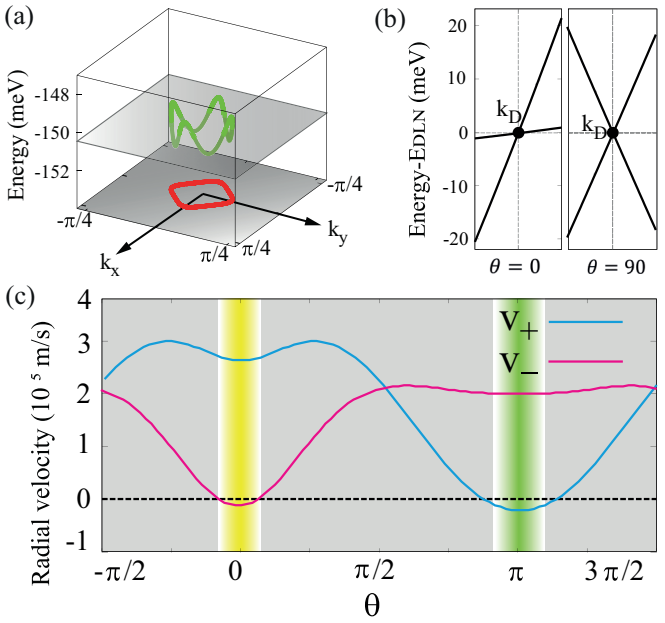

FIG. 4. (a) A DNL (red) in energy-momentum space. A DLN is placed on the $k_z = 0$ plane, encircling the Γ point. The energy bands disperse along the DLN (green line) in the energy range $\Delta E_{\mathrm{DLN}} \approx 0.002$ eV. (b) Energy dispersions at a point (at $\boldsymbol{k}_D$) in the type-II DLN drawn along the q_ρ (left panel) and q_z (right panel) directions. (c) Radial band velocities of the valence and conduction bands calculated as a function of the azimuthal angle θ on the q_ρ-q_z plane [see Fig. 1(c)]. The pink (blue) curve represents the velocity of the valence (conduction) band. The valence (conduction) band undergoes sign change outside (inside) of the DLN across the critical angle $\theta \approx \pm 13.0^\circ$ ($\theta \approx 180^\circ \pm 16.0^\circ$).

forming the DLN and clarify the geometry of the DLN in the BZ. Next, we discuss the topological protection by calculating $\mathbb{Z}_2$ topological invariants that dictate the presence of DLNs [25]. Finally, we show the type-II nature of the DLN. For this purpose, we construct a $\boldsymbol{k} \cdot \boldsymbol{p}$ Hamiltonian and an explicit tight-binding model that reproduce the DFT band structure, and apply the type-I/type-II criterion derived in Sec. II, which confirms the type-II class. For further demonstration of the type-II nature, we present the unconventional linear dispersion occurring along principal axes from our DFT calculations. We also calculate the numerical value of the principal curvatures, resulting in Gaussian curvatures with opposite sign, which reaffirms the type-II nature.

A. DLN

Careful inspection of the band structure in the entire BZ allows us to find a single DLN encircling Γ that lies on the $k_z = 0$ plane as shown in Fig. 4(a). The DLN is located at $E_{\mathrm{DLN}} \approx -0.15$ eV below the Fermi energy, with dispersion in the energy range of $\Delta E_{\mathrm{DLN}} \approx 0.002$. The protection of the DLN is twofold. First, lying on the $k_z = 0$ mirror-invariant plane, the DLN is protected by $\mathcal{M}_z$ with the conduction and valence bands having different mirror eigenvalues ± 1. In addition, the DLN is also topologically protected by inversion $\mathcal{P}$ and time-reversal $\mathcal{T}$ symmetries [25,26]. Judging from the group representation of the Bloch states forming the DLN,

TABLE I. Parameters of the $\boldsymbol{k}\cdot\boldsymbol{p}$ Hamiltonian that best match the DFT band structures of pristine and 5% strained Na_3N. Here, k_ρ and k_z are in units of $2\pi/a$ and $2\pi/c$, respectively, and the parameters are in units of eV.

Parameter	Pristine	5% strained
a_1	5.00	5.00
b_1	4.60	4.60
a_2	5.00	4.00
b_2	4.60	3.80
v	0.00	1.05
k_D	0.00	0.14

we find the band inversion at Γ between the A_{2u} and the A_{1g} states, which are odd- and even-parity eigenstates of inversion $\mathcal{P}$, respectively. These two states are also mirror eigenstates having opposite parities, leading to the mirror-protected band crossing on the mirror-invariant plane $k_z = 0$. The presence and geometric shape of a DLN in momentum space are dictated by the $\mathbb{Z}_2$ topological indices $(\nu_0;\nu_1\nu_2\nu_3)$ as discussed in Ref. [25]. We find $(\nu_0;\nu_1\nu_2\nu_3) = (1;000)$ for strained Na_3N from parity analysis at the time-reversal invariant momenta (TRIMs) $(\Gamma, 2X, M, 2R, A, Z)$, which agree with the existence and shape of the DLN. In detail, $(\nu_0;\nu_1\nu_2\nu_3) = (1;000)$ enforces an odd number of DLNs to thread the half $\mathcal{T}$-invariant plane containing Γ. This is fulfilled by the DLN encircling the Γ lying on the $k_z = 0$ plane.

B. $\boldsymbol{k}\cdot\boldsymbol{p}$ analysis and type-II nature

In this section, we construct the $\boldsymbol{k}\cdot\boldsymbol{p}$ Hamiltonian that describes the DLN and confirm its type-II nature. The $\boldsymbol{k}\cdot\boldsymbol{p}$ Hamiltonian near Γ can be constructed such that it respects the O_h^1 little group symmetries of Γ on the basis $\left(\frac{1}{0}\right) = A_{2u}$ and $\left(\frac{0}{1}\right) = A_{1g}$:

$$H = \left[a_1\left(k_\rho^2 - k_D^2\right) + a_2 k_z^2\right] + v k_z \sigma_y + \left[b_1\left(k_\rho^2 - k_D^2\right) + b_2 k_z^2\right]\sigma_z. \tag{10}$$

Here $k_\rho = \sqrt{k_x^2 + k_y^2}$, σ_j's are the Pauli matrices in the (A_{2u}, A_{1g}) basis, and a_1, a_2, b_1, and b_2 are constants. The DLN forms along a circle $k_\rho = k_D$ on the $k_z = 0$ plane. The first term in Eq. (10) induces tilting that enables the type-II nature of the DLN. The $a_1 k_D^2$ term sets the energy of the DLN to 0 by convention within the $\boldsymbol{k}\cdot\boldsymbol{p}$ model. The best match to the DFT band structure in the vicinity of the Γ point for pristine and 5% strained Na_3N is found when using the parameters listed in Table I [88]. In the pristine case, where $a_1 = a_2$, $b_1 = b_2$, $v = 0$, and $k_D = 0$, the energy states are degenerate at Γ $[(k_\rho, k_z) = (0,0)]$, exhibiting an isotropic band structure originating from the cubic symmetry. The tensile strain reduces the cubic symmetry to tetragonal symmetry, described by nonzero values for the velocity v and the radius of the DLN k_D, as well as the difference between the values of $a_1(b_1)$ and $a_2(b_2)$.

As previously pointed out in Sec. II, the $\boldsymbol{k}\cdot\boldsymbol{p}$ Hamiltonian can be expanded in $\boldsymbol{q} = \boldsymbol{k} - \boldsymbol{k}_D$ in the vicinity of a point on the DLN $\boldsymbol{k}_D$

$$H = 2a_1 k_D q_\rho + v q_z \sigma_y + 2b_1 k_D q_\rho \sigma_z, \tag{11}$$

which is of the same form as Eq. (3) with the principal axes q_ρ and q_z. The type-II criterion previously worked out in Sec. II is simplified as

$$a_1^2 > b_1^2, \tag{12}$$

which is consistent with the previously proposed type-I/type-II classification of DLNs [65]. As shown in Table I, 5% strained Na_3N indeed satisfies Eq. (12), thus confirming the type-II DLN semimetal phase.

The type-II nature is further illustrated from the shape of Dirac cones. Figure 4(b) illustrates the band structures drawn along the q_ρ $(\theta = 0^\circ)$ and q_z $(\theta = 90^\circ)$ directions, which are the principal axes of the $\boldsymbol{k}\cdot\boldsymbol{p}$ Hamiltonian. We find that the unconventional (left panel) and conventional (right panel) linear dispersions coexist in the vicinity of the Dirac point, which is a characteristic of the unconventional type-II DLN. Figure 4(c) shows the radial band velocities $v_\pm$ around the DLN as a function of $\theta = [0, 2\pi]$ calculated from the DFT band structures. A conventional (an unconventional) linear dispersion resides in the gray (yellow and green) region, resulting in $v_+v_- > 0$ $(v_+v_- < 0)$, which proves the sign change in the band velocities. Additionally, it is manifested that either the conduction or the valence band is a saddle-shaped band undergoing the sign flip of the radial-band velocity, resulting in $K_+K_- < 0$. This is a characteristic of the radial-band velocities present only in type-II DLN semimetals. In a type-I DLN semimetal, $v_\pm$ should be positive for the entire range of $\theta = [0, 2\pi]$, resulting in $K_+K_- > 0$.

V. TIGHT-BINDING MODEL ANALYSIS

The tight-binding model is a useful way to develop the low-energy effective theory for the DLN. We construct it using the basis of p orbitals of the N atom and the s orbital of Na. The basis orbitals are thus (N p_x, N p_y, N p_z, Na-x s, Na-y s, Na-z s), where Na-x is the Na atom at $(a/2, 0, 0)$, Na-y at $(0, a/2, 0)$, and Na-z at $(0, 0, c/2)$, respectively. We arrive at the tight-binding Hamiltonian written in block form:

$$\mathcal{H} = \begin{pmatrix} \mathcal{H}_{\mathrm{N}} & \mathcal{H}_{\mathrm{N\text{-}Na}} \\ H^\dagger_{\mathrm{N\text{-}Na}} & \mathcal{H}_{\mathrm{Na}} \end{pmatrix}. \tag{13}$$

The 3×3 submatrices $\mathcal{H}_{\mathrm{N}}$ and $\mathcal{H}_{\mathrm{Na}}$ concern the three p orbitals of N and the three inequivalent s orbitals of Na, respectively. $\mathcal{H}_{\mathrm{Na\text{-}N}}$ is their hybridization. In detail,

$$\mathcal{H}_{\mathrm{N}} = \begin{pmatrix} E_{\mathrm{N},p} - 2t_{3pp\sigma\parallel}c_x + 2t_{3pp\pi\parallel}c_y + 2t_{3pp\pi\perp}c_z & 0 & 0 \\ 0 & E_{\mathrm{N},p} + 2t_{3pp\pi\parallel}c_x - 2t_{3pp\sigma\parallel}c_y + 2t_{3pp\pi\perp}c_z & 0 \\ 0 & 0 & E_{\mathrm{N},p} + 2t_{3pp\pi\parallel}c_x + 2t_{3pp\pi\parallel}c_y - 2t_{3pp\sigma\perp}c_z \end{pmatrix},$$

TABLE II. On-site energies and hopping integrals for pristine Na_3N.

On-site energy	Value (eV)
$E_{N,p}$	-2.45
$E_{Na,s}$	$+0.85$
Hopping integral	
$t_{sp\sigma}$	-1.00
t_{2ss}	-0.47
$t_{3pp\sigma}$	-0.13
$t_{3pp\pi}$	-0.015

$$\mathcal{H}_{Na} = \begin{pmatrix} E_{Na,s\parallel} & 4t_{2ss\parallel}c_{x2}c_{y2} & 4t_{2ss\perp}c_{x2}c_{z2} \\ 4t_{2ss\parallel}c_{x2}c_{y2} & E_{Na,s\parallel} & 4t_{2ss\perp}c_{y2}c_{z2} \\ 4t_{2ss\perp}c_{x2}c_{z2} & 4t_{2ss\perp}c_{y2}c_{z2} & E_{Na,s\perp} \end{pmatrix},$$

$$\mathcal{H}_{N\text{-}Na} = \begin{pmatrix} 2it_{sp\sigma\parallel}s_{x2} & 0 & 0 \\ 0 & 2it_{sp\sigma\parallel}s_{y2} & 0 \\ 0 & 0 & 2it_{sp\sigma\perp}s_{z2} \end{pmatrix}. \quad (14)$$

Here, abbreviations are used for $c_{x(y)} = \cos k_{x(y)}$, $c_z = \cos k_z$, $c_{x(y)2} = \cos(k_{x(y)}/2)$, $c_{z2} = \cos(k_z/2)$, $s_{x(y)2} = \sin(k_{x(y)}/2)$, and $s_{z2} = \sin(k_z/2)$. The on-site energy of the N p orbitals is denoted $E_{N,p}$. Similarly, the on-site energies for the Na-$x(y)$ and Na-z orbitals are denoted $E_{Na,s\parallel}$ and $E_{Na,s\perp}$, respectively. Note that $E_{Na,s\parallel}$ and $E_{Na,s\perp}$ are inequivalent under the strain due to a different Coulomb potential felt by the Na s orbitals.

We consider the hopping between the basis orbitals up to third-nearest neighbors in the pristine and strained crystal structure. For nearest-neighbor hopping, the hopping integral between the $p_{x(y,z)}$ orbital at the origin and the s orbital of the Na-$x(y,z)$ atom is denoted $t_{sp\sigma,x(y,z)}$. In the pristine case, the cubic symmetry enforces $t_{sp\sigma,x} = t_{sp\sigma,y} = t_{sp\sigma,z} = t_{sp\sigma}$. In the strained case, the lowered symmetry differentiates $t_{sp\sigma,z}$ from $t_{sp\sigma,x} = t_{sp\sigma,y}$. We denote $t_{sp\sigma,x(y)}$ as $t_{sp\sigma\parallel}$ and $t_{sp\sigma,z}$ as $t_{sp\sigma\perp}$, respectively. Second-nearest-neighbor hopping takes place between Na-x and Na-y or between equivalent Na atoms. The corresponding hopping integrals are denoted as $t_{2ss\parallel}$ for Na-x s to Na-y s and as $t_{2ss,\perp}$ for Na-x s to Na-z s or Na-y s to Na-z s. One can expect $t_{2ss\parallel} = t_{2ss\perp}$ only for the pristine cubic crystal of Na_3N. Third-nearest-neighbor hopping takes place between the p orbitals of N atoms in adjacent unit cells [distanced by $\pm R_{x(y,z)}$], parameterized by the hopping integrals $t_{3pp,x(y,z)}$. Considering π and σ symmetry between p orbitals, we obtain the constraints for the pristine and strained cases. In the pristine case, there is no difference among the x, y, and z directions. Therefore, there are only two types of distinct hopping integrals, $t_{3pp\sigma}$ and $t_{3pp\pi}$. In contrast, there are four third-neighbor hopping integrals, $t_{3pp\sigma\parallel}$, $t_{3pp\sigma\perp}$, $t_{3pp\pi\parallel}$, and $t_{3pp\pi\perp}$, in the strained case. In the tetragonal-symmetric case, $t_{3pp\sigma(\pi)\parallel}$ represents $t_{3pp\sigma(\pi),x}$ and $t_{3pp\sigma(\pi),y}$. On the other hand, $t_{3pp\sigma(\pi),\perp}$ represents $t_{3pp\sigma(\pi),z}$ The on-site energies and hopping integrals for pristine (strained) cases are listed in Table II (Table III). A negative value of the hopping parameter $t_{3pp\pi\parallel}$ is responsible for the DLN belonging to the type-II class. A type-I DLN occurs for positive $t_{3pp\pi\parallel}$.

TABLE III. On-site energies and hopping integrals for 5% strained Na_3N.

On-site energy	Value (eV)
$E_{N,p}$	-2.45
$E_{Na,s\parallel}$	$+0.85$
$E_{Na,s\perp}$	$+0.92$
Hopping integral	
$t_{sp\sigma\parallel}$	-0.95
$t_{sp\sigma\perp}$	-0.95
$t_{2ss\parallel}$	-0.46
$t_{2ss\perp}$	-0.47
$t_{3pp\sigma\parallel}$	-0.13
$t_{3pp\sigma\perp}$	-0.205
$t_{3pp\pi\parallel}$	-0.014
$t_{3pp\pi\parallel}$	-0.025

Close fits to both pristine and strained DFT bands are achieved in Fig. 5 using the tight-binding parameters in Table II. Near the Γ point, the DLN occurs. The tight-binding model corroborates the following DFT results. The line node is formed via the band inversion between the odd-parity eigenstate composed of the N p_z orbital and the even-parity eigenstate composed of the three s orbitals from Na-x, Na-y, and Na-z. In both cases, the even parity state is below the odd-parity eigenstate at Γ, while the even-parity state is above the odd-parity eigenstates at the other seven TRIM points. The strain opens the band gap between $n_{occ} = 3$ and $n_{occ} = 4$ states at the eight TRIM points, resulting in a nontrivial $\mathcal{Z}_2$ topological invariant. Based on the tight-binding parameters in Table III we also reproduced the same $\mathcal{Z}_2$ topological invariants as the DFT results.

VI. PHYSICAL MANIFESTATIONS

In this section, we discuss feasible ways to detect the type-II DNL character of strained Na_3N. Two physical manifestations are suggested: topological surface states and optical conductivity, which we discuss in the following subsections. We suggest that the two can help clarify the topological and type-II nature of the DLN hosted in strained Na_3N, respectively.

A. Topological surface states

A topologically protected DLN features drumheadlike surface states [5,25,26,37]. We confirm this topological char-

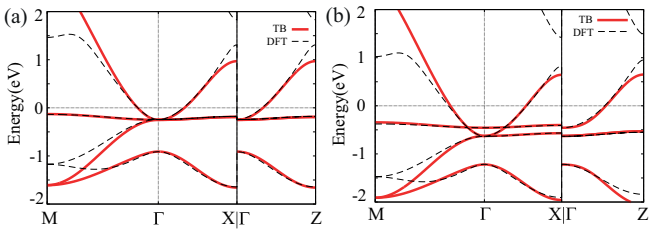

FIG. 5. Tight-binding and DFT band structures for (a) pristine and (b) 5% strained Na_3N.

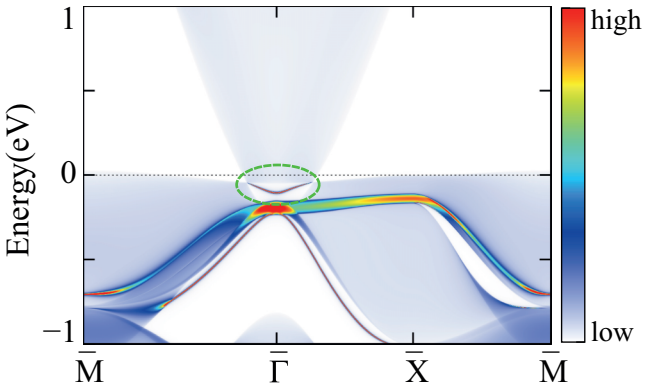

FIG. 6. Surface band structure of 5% strained Na_3N calculated from the maximally localized Wannier Hamiltonian. Topological surface states appear inside the bulk gap near the Γ point as a bright branch inside a green circle. The color scheme shows the density of states at a given energy and k points. Red (blue) indicates a high (low) density of the surface projected states.

acteristic of the surface energy spectra using the surface Green's function. Figure 6 shows the resultant surface band structure of the (001) surface for a semi-infinite slab of Na_3N, drawn along projected high-symmetry lines following the $\bar{M}$-$\bar{\Gamma}$-$\bar{X}$-$\bar{M}$ path of the square lattice. As the bulk DLN is parallel to the (001) surface, the interior region of the DLN is projected to a finite area of the surface BZ near Γ. The region shaded a bluish color in Fig. 6 shows the projected bulk states. The type-II nature is revealed in the unconventional (tilted) linear dispersion appearing on $\bar{M}$-$\bar{\Gamma}$ and $\bar{\Gamma}$-$\bar{X}$, as shown in Fig. 6.

The high-intensity branch connecting the two crossing points is the topological surface states. They appear in the interior region of the projected DLN enclosing $\bar{\Gamma}$, indicated by the green circle. This explicitly proves the topological nature of strained Na_3N. As discussed in Ref. [25], the curvature of the surface states is in part determined by the harmonic average of the curvatures of the conduction and valence bands. Our DFT calculations also feature this, yet due to the same sign of the curvature for the conduction and valence bands, the topological surface states appear more dispersive than the nearly flat surface bands of a type-I DLN. This is another characteristic feature of a type-II DLN semimetal captured in the surface energy spectrum. We also note that there is a high-intensity contribution from the bulk states to the surface energy spectrum, originating from nondispersive bulk bands along the z direction, comprising mainly the N p_x and p_y orbitals. We suggest that these nontopological states should be well separated from the topological drumheadlike states when the strain is applied beyond the 4% tensile strain, making a clear distinction between the topological surface states and the bulk trivial states.

B. Optical conductivity

The optical conductivity of DLN semimetals has been studied in the literature and is known to exhibit a flat behavior at low frequencies, below the nodal ring energy scale [89,90]. In this subsection, we investigate the optical responses of Na_3N in both the pristine and the strained cases. We demonstrate that the strain results in a qualitative change in the optical conductivity, suggesting that the optical signal of Na_3N could serve as an experimental footprint for the occurrence of the DLN under strain.

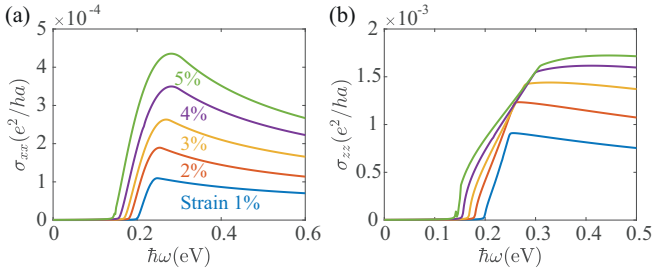

FIG. 7. Interband optical conductivities of Na_3N as a function of the epitaxial tensile strain. Both (a) σ_{xx} and (b) σ_{zz} show a sudden jump, which occurs near the energy of the DLN. The optical conductivity vanishes in the pristine case because interband transitions are forbidden.

To obtain the optical conductivity, we evaluate the Kubo formula using the two-band effective model in Eq. (10). In the linear response and clean limit, the Kubo formula for the optical conductivity [91] is written as

$$\sigma_{ij}(\omega) = -\frac{ie^2}{\hbar}\sum_{s,s'}\int \frac{d^3k}{(2\pi)^3}\frac{f_{s,\boldsymbol{k}} - f_{s',\boldsymbol{k}}}{\varepsilon_{s,\boldsymbol{k}} - \varepsilon_{s',\boldsymbol{k}}} \times \frac{M_i^{ss'}(\boldsymbol{k})M_j^{s's}(\boldsymbol{k})}{\hbar\omega + \varepsilon_{s,\boldsymbol{k}} - \varepsilon_{s',\boldsymbol{k}} + i0^+}, \quad (15)$$

where $i, j = x, y, z$, $\varepsilon_{s,\boldsymbol{k}}$ and $f_{s,\boldsymbol{k}} = 1/[1 + e^{(\varepsilon_{s,\boldsymbol{k}}-\mu)/k_BT}]$ are the eigenenergy and the Fermi distribution function for the band index $s = \pm$ and wave vector $\boldsymbol{k}$, respectively, μ is the chemical potential, and $M_i^{ss'}(\boldsymbol{k}) = \langle s, \boldsymbol{k}|\hbar\hat{v}_i|s', \boldsymbol{k}\rangle$ with the velocity operator $\hat{v}_i = \frac{1}{\hbar}\frac{\partial\hat{H}}{\partial k_i}$.

We first consider the pristine case. By applying the pristine parameters in Table I to Eq. (10), we obtain the effective Hamiltonian $H = a_1|\boldsymbol{k}|^2 + b_1|\boldsymbol{k}|^2\sigma_z$. The energy eigenstates and the velocity operator can be represented as the eigenstates of σ_z and $\hat{v}_i = \frac{2k_i}{\hbar}(a_1 + b_1\sigma_z)$, respectively. Using these, it is readily shown that the matrix element $M_i^{ss'}(\boldsymbol{k}) \propto \delta_{ss'}$ and, thus, interband transitions are forbidden in the pristine case. In contrast, in the strained case, interband transitions are allowed, thus resulting in the nonzero optical response. The nonzero velocity term [$vk_z\sigma_y$ in Eq. (10)] makes the wave functions $\boldsymbol{k}$ dependent, leading to the nonvanishing matrix element for the interband transitions. We have calculated the interband optical conductivity as a function of the strain; results for 1% to 5% are summarized in Fig. 7 [92]. Notably, both σ_{xx} and σ_{zz} exhibit a sudden increase at around $\hbar\omega = \mu - E_{\mathrm{DLN}}$ for a given strain, which corresponds to the size of the optical gap arising from the Pauli blocking. In detail, the conduction band is partially filled near the DLN as the chemical potential is placed above the energy of the DLN ($\mu > E_{\mathrm{DLN}}$). In order for an optical transition to occur, an electron in an occupied state of the valence band, whose energy is $\sim E_{\mathrm{DLN}}$ as the valence band is nearly flat on the k_x-k_y plane, as shown in the inset in Fig. 3(b), should acquire the energy to overcome

the chemical potential (the Pauli blocking) and transit to an unoccupied state of the conduction band. The threshold for the optical conductivity is decreased as the strain increases since the energy of the nearly flat valence band is increased. Thus, the energy of the DLN (E_{DLN}) increases below the chemical potential, leading to the decrease in the offset energy $\mu - E_{\mathrm{DLN}}$. Such a qualitative change upon straining of the material, i.e., a sudden rise in the optical conductivity, is a key signature of the emergence of the Dirac line node induced by the strain. We note that other kinks in Fig. 7(b) appear near $\hbar\omega \sim 0.25$ eV, which originate from the topological change in the phase space where interband transitions are allowed [89].

VII. DISCUSSION AND SUMMARY

In summary, we have characterized a type-II topological DLN semimetal and proposed strained Na_3N as its material realization. We have shown that type-I/type-II DLNs can be classified in an equivalent manner by the mathematical formalism governing any one of three features: the Fermi surface geometry, the sign inversion of the band velocity, or the band curvature. We believe that these connections provide a fundamental and clear picture for the type-I/type-II classification of DLNs. In addition, the type-II condition represented in terms of the band velocity should provide a computationally convenient way to determine the types of DLNs. Furthermore, our extensive DFT calculations predict that a type-II DLN semimetal should be realized in Na_3N under epitaxial strain. We propose the drumhead surface state spectrum and optical conductivity as two key physical manifestations indicating the existence of a type-II DLN in strained Na_3N. In particular, the optical response is expected to undergo a sudden jump under strain due to the creation of a DLN, while the interband transition in pristine Na_3N is suppressed by the selection rule. This feature should serve as experimental evidence of the type-II DLN semimetal phase hosted in strained Na_3N.

Encouragingly, the synthesis of pristine Na_3N has been reported in the literature [93–95]. However, to the best of our knowledge, the literature disagrees with our DFT calculation. For example, the optical response of Na_3N reported in Ref. [86] for visible light and near-IR spectra results in a sizable optical band gap, 1.6–2.0 eV. Also, first-principles calculations based on self-interaction correction (SIC) and G_0W_0 methods support the experiment [87]. Clearly, they stand in contrast to our calculation based on the LDA and HSE. On the other hand, the band-gap calculation based on the HSE06 hybrid functional, which reproduces experimental band gaps with a high degree of accuracy in some systems [96–100], also shows metallic behavior in line with the LDA and GGA calculations (see Appendix A).

As described in Sec. IV, the inversion of the s and p bands at the Γ point is a key ingredient for the formation of a DLN as well as the band gap. The band inversion is captured by the LDA or HSE06 calculation but, apparently, not by the previous SIC or G_0W_0 calculations. To better understand the origin of this discrepancy, we made tight-binding fits to the band structures of HSE06, SIC, and G_0W_0 as shown in Appendix A. Compared to the estimation by the LDA results, other calculations showed an increase in the on-site energy of Na s orbitals, $E_{\mathrm{Na},s}$: by $+0.65$, $+1.10$, and 2.25 eV, respectively. The dramatic increase in $E_{\mathrm{Na},s}$ in the case of SIC and G_0W_0 is presumably responsible for the lack of band inversion at the Γ point, as well as the consequent absence of a DLN. Tight-binding models deduced from fits of SIC and G_0W_0 bands gave the trivial topological number, as expected.

We believe that the metallicity of Na_3N yet requires further confirmation via accurate band-gap measurements, such as absorption spectra with low-energy photon energies or transport experiments. The previous experiment was performed using Na_3N powders, which could potentially contain excessive Na, as mentioned in Ref. [86]. Therefore, the existing discrepancy regarding the metallicity of Na_3N is a source for pursuing careful experimental verification of the electronic properties of this material, given our finding of topological nodal semimetallic behavior with a novel velocity dispersion under strain.

ACKNOWLEDGMENTS

D.K. was supported by the Samsung Science and Technology Foundation (Project No. SSTF-BA1701-07) and Basic Science Research Program through the National Research Foundation of Korea (NRF) funded by the Ministry of Education (Grant No. NRF-2018R1A6A3A11044335). S.A. and H.M. were supported by an NRF grant funded by the Korea government (MSIT; No. 2018R1A2B6007837) and the Creative-Pioneering Researchers Program through Seoul National University (SNU). J.H.H. was supported by the Samsung Science and Technology Foundation under Project No. SSTF-BA1701-07. Y.K. was supported by the Institute for Basic Science (Grant No. IBS-R011-D1) and an NRF grant funded by the Korea government [Ministry of Science, ICT & Future Planning (MSIP); No. NRF-2017R1C1B5018169]. Computational calculations were performed using the resources of the Korea Institute of Science and Technology Information (KISTI).

APPENDIX A: BAND STRUCTURE CALCULATION WITH OTHER TYPES OF EXCHANGE-CORRELATION FUNCTIONALS

Figures 8(a) and 8(b), respectively, show the band structures of pristine Na_3N obtained using the GGA and HSE06 exchange-correlation functionals. Both electronic band structures are calculated as metallic, similar to the LDA result. In contrast, the literature reports band structures of Na_3N calculated using the SIC and G_0W_0 [87] which are semiconducting. These contrasting results reflect a well-known band-gap issue of DFT functionals. We attribute this disagreement mainly to the different description of the on-site energies of the Na s orbital. We find five sets of tight-binding parameters that reproduce the DFT results with each of the five schemes (LDA, GGA, HSE06, SIC, and G_0W_0) (see Fig. 8 for the GGA, HSE06, SIC, and G_0W_0 band structures). The on-site energies of the Na s orbitals for the GGA, HSE06, SIC, and G_0W_0 results are increased by 0.00, 0.65, 1.10, and 2.25 eV with respect to the LDA result. The differences in on-site

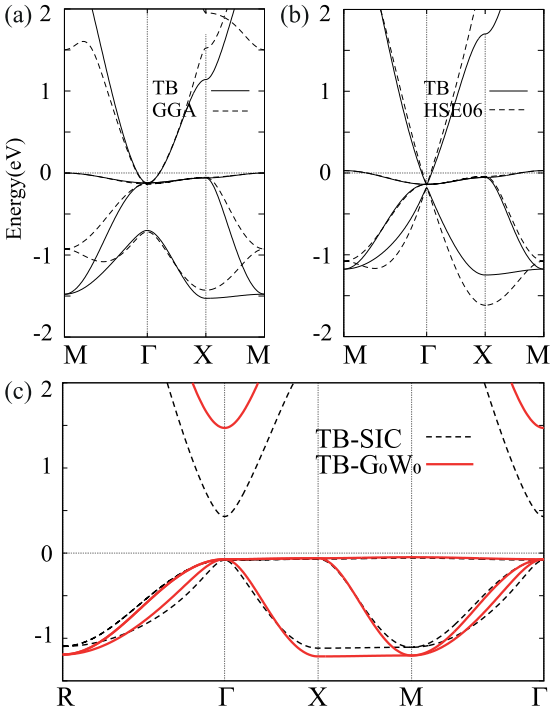

FIG. 8. (a) GGA band structure (dashed line) of pristine Na_3N and tight-binding band structure reproducing the GGA result (solid line). (b) HSE06 band structure (dashed line) of pristine Na_3N and tight-binding band structure reproducing the HSE06 result (solid line). (c) Tight-binding band structure reproducing the SIC and G_0W_0 results in [87].

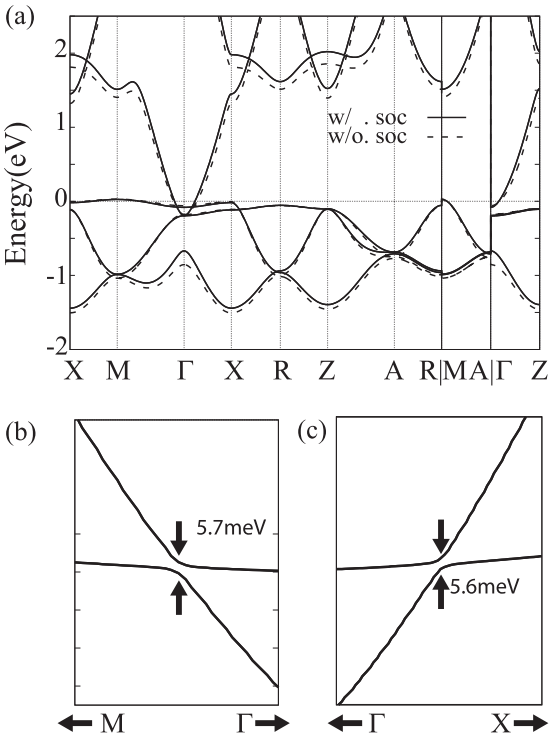

FIG. 9. (a) Electronic band structure of strained Na_3N with and without SOC. The SOC band is represented by the solid line; the non-SOC band, by the dashed line. Magnified views of the band structure on (b) Γ-M and (c) Γ-X. The size of the SOC gap on Γ-X (Γ-M) is calculated as ∼5.6 meV (∼5.7 meV).

energies $E_{\mathrm{Na},s}$ lead to the semimetallic (semiconducting) band structures of the LDA, GGA, and HSE06 (SIC, G_0W_0) $E_{\mathrm{N},p}$. Accordingly, we find a DLN in the LDA, GGA, and HSE06 results under strain, but not in the SIC and G_0W_0 calculations.

To resolve the discrepancy of different DFT methods, and to confirm the type-II DLN semimetal phase in Na_3N under strain, we emphasize that a careful set of new experiments on both pristine and strained Na_3N is crucial. A previous optical conductivity experiment on the powdered Na_3N tentatively reached a conclusion in favor of an energy gap at the Γ point [86], but we feel that significant refinement of both the sample preparation and the measurement are still in demand, preferably on single-crystalline samples.

APPENDIX B: EFFECT OF SPIN-ORBIT COUPLING

For the sake of completeness of the study, we calculate the electronic band structure of Na_3N with SOC shown in Fig. 9(a). Indeed the effect of SOC is negligibly weak. It is found that SOC opens a tiny band gap along the entire DLN. As shown in Figs. 9(b) and 9(c), a band gap opens by ∼5.6 and ∼5.7 meV on the high-symmetry Γ-M and Γ-X lines, respectively. Considering SOC, strained Na_3N can be considered a strong topological insulator protected by time-reversal symmetry. We confirm the nontrivial topological insulator phase induced by SOC by calculating the $\mathbb{Z}_2$ invariants using parity eigenvalues. This calculation results in (1;000), indicating a strong topological insulator.

APPENDIX C: PARAMETERS OF THE $\boldsymbol{k}\cdot\boldsymbol{p}$ HAMILTONIAN

In Table IV, we present the parameters of the $\boldsymbol{k}\cdot\boldsymbol{p}$ Hamiltonians for the pristine and the 1%, 2%, 3%, 4%, and 5% strained Na_3N which best reproduce the corresponding first-principles band structures. These parameters were used to calculate the optical conductivities presented in Sec. VI B.

TABLE IV. Parameters of the $\boldsymbol{k}\cdot\boldsymbol{p}$ Hamiltonians for pristine and 1%, 2%, 3%, 4%, and 5% strained Na_3N.

		Strained				
Parameter (eV)	Pristine	1%	2%	3%	4%	5%
a_1	5.00	5.00	5.00	5.00	5.00	5.00
b_1	4.60	4.60	4.60	4.60	4.60	4.60
a_2	5.00	4.82	4.64	4.46	4.28	4.00
b_2	4.60	4.46	4.32	4.18	4.04	3.80
v	0.00	0.65	0.78	0.92	1.02	1.05
k_D	0.00	0.070	0.095	0.109	0.125	0.140
$\mu - E_{\mathrm{DLN}}$	0.248	0.210	0.190	0.178	0.165	0.150

[1] F. Arnold, C. Shekhar, S.-C. Wu, Y. Sun, R. D. dos Reis, N. Kumar, M. Naumann, M. O. Ajeesh, M. Schmidt, A. G. Grushin *et al.*, Nat. Commun. **7**, 11615 (2016).

[2] C.-L. Zhang, S.-Y. Xu, I. Belopolski, Z. Yuan, Z. Lin, B. Tong, G. Bian, N. Alidoust, C.-C. Lee, S.-M. Huang *et al.*, Nat. Commun. **7**, 10735 (2016).

[3] H. Li, H. He, H.-Z. Lu, H. Zhang, H. Liu, R. Ma, Z. Fan, S.-Q. Shen, and J. Wang, Nat. Commun. **7**, 10301 (2016).

[4] L. P. He, X. C. Hong, J. K. Dong, J. Pan, Z. Zhang, J. Zhang, and S. Y. Li, Phys. Rev. Lett. **113**, 246402 (2014).

[5] A. A. Burkov, M. D. Hook, and L. Balents, Phys. Rev. B **84**, 235126 (2011).

[6] X. Wan, A. M. Turner, A. Vishwanath, and S. Y. Savrasov, Phys. Rev. B **83**, 205101 (2011).

[7] K.-Y. Yang, Y.-M. Lu, and Y. Ran, Phys. Rev. B **84**, 075129 (2011).

[8] G. Xu, H. Weng, Z. Wang, X. Dai, and Z. Fang, Phys. Rev. Lett. **107**, 186806 (2011).

[9] B. Singh, A. Sharma, H. Lin, M. Z. Hasan, R. Prasad, and A. Bansil, Phys. Rev. B **86**, 115208 (2012).

[10] S.-M. Huang, S.-Y. Xu, I. Belopolski, C.-C. Lee, G. Chang, B. Wang, N. Alidoust, G. Bian, M. Neupane, C. Zhang *et al.*, Nat. Commun. **6**, 7373 (2015).

[11] S.-Y. Xu, I. Belopolski, N. Alidoust, M. Neupane, G. Bian, C. Zhang, R. Sankar, G. Chang, Z. Yuan, C.-C. Lee *et al.*, Science **349**, 613 (2015).

[12] S.-Y. Xu, C. Liu, S. K. Kushwaha, R. Sankar, J. W. Krizan, I. Belopolski, M. Neupane, G. Bian, N. Alidoust, T.-R. Chang *et al.*, Science **347**, 294 (2015).

[13] H. Weng, C. Fang, Z. Fang, B. A. Bernevig, and X. Dai, Phys. Rev. X **5**, 011029 (2015).

[14] B. Lv, H. Weng, B. Fu, X. Wang, H. Miao, J. Ma, P. Richard, X. Huang, L. Zhao, G. Chen *et al.*, Phys. Rev. X **5**, 031013 (2015).

[15] N. Xu, H. M. Weng, B. Q. Lv, C. E. Matt, J. Park, F. Bisti, V. N. Strocov, D. Gawryluk, E. Pomjakushina, K. Conder *et al.*, Nat. Commun. **7**, 11006 (2016).

[16] S.-Y. Xu, N. Alidoust, I. Belopolski, Z. Yuan, G. Bian, T.-R. Chang, H. Zheng, V. N. Strocov, D. S. Sanchez, G. Chang *et al.*, Nat. Phys. **11**, 748 (2015).

[17] S. Jia, S.-Y. Xu, and M. Z. Hasan, Nat. Mater. **15**, 1140 (2016).

[18] S.-Y. Xu, Y. Xia, L. A. Wray, S. Jia, F. Meier, J. H. Dil, J. Osterwalder, B. Slomski, A. Bansil, H. Lin *et al.*, Science **332**, 560 (2011).

[19] Z. K. Liu, B. Zhou, Y. Zhang, Z. J. Wang, H. M. Weng, D. Prabhakaran, S.-K. Mo, Z. X. Shen, Z. Fang, X. Daiz *et al.*, Science **343**, 864 (2014).

[20] Z. Wang, Y. Sun, X.-Q. Chen, C. Franchini, G. Xu, H. Weng, X. Dai, and Z. Fang, Phys. Rev. B **85**, 195320 (2012).

[21] S. M. Young, S. Zaheer, J. C. Y. Teo, C. L. Kane, E. J. Mele, and A. M. Rappe, Phys. Rev. Lett. **108**, 140405 (2012).

[22] S. Borisenko, Q. Gibson, D. Evtushinsky, V. Zabolotnyy, B. Büchner, and R. J. Cava, Phys. Rev. Lett. **113**, 027603 (2014).

[23] Z. Wang, H. Weng, Q. Wu, X. Dai, and Z. Fang, Phys. Rev. B **88**, 125427 (2013).

[24] Z. K. Liu, J. Jiang, B. Zhou, Z. J. Wang, Y. Zhang, H. M. Weng, D. Prabhakaran, S.-K. Mo, H. Peng, P. Dudin *et al.*, Nat. Mater. **13**, 677 (2014).

[25] Y. Kim, B. J. Wieder, C. L. Kane, and A. M. Rappe, Phys. Rev. Lett. **115**, 036806 (2015).

[26] R. Yu, H. Weng, Z. Fang, X. Dai, and X. Hu, Phys. Rev. Lett. **115**, 036807 (2015).

[27] R. Yu, Z. Fang, X. Dai, and H. Weng, Front. Phys. **12**, 127202 (2016).

[28] C. Fang, H. Weng, X. Dai, and Z. Fang, Chin. Phys. B **25**, 117106 (2016).

[29] H. Weng, X. Dai, and Z. Fang, J. Phys.: Condens. Matter **28**, 303001 (2016).

[30] C.-K. Chiu, J. C. Y. Teo, A. P. Schnyder, and S. Ryu, Rev. Mod. Phys. **88**, 035005 (2016).

[31] C. Fang, Y. Chen, H.-Y. Kee, and L. Fu, Phys. Rev. B **92**, 081201 (2015).

[32] Q. Xu, R. Yu, Z. Fang, X. Dai, and H. Weng, Phys. Rev. B **95**, 045136 (2017).

[33] H. Huang, J. Liu, D. Vanderbilt, and W. Duan, Phys. Rev. B **93**, 201114 (2016).

[34] S. M. Young, S. Manni, J. Shao, P. C. Canfield, and A. N. Kolmogorov, Phys. Rev. B **95**, 085116 (2017).

[35] J. Zhao, R. Yu, H. Weng, and Z. Fang, Phys. Rev. B **94**, 195104 (2016).

[36] Y. Du, F. Tang, D. Wang, L. Sheng, E.-j. Kan, C.-G. Duan, S. Y. Savrasov, and X. Wan, Quant. Mater. **2**, 3 (2017).

[37] H. Weng, Y. Liang, Q. Xu, R. Yu, Z. Fang, X. Dai, and Y. Kawazoe, Phys. Rev. B **92**, 045108 (2015).

[38] Y. Chen, Y. Xie, S. A. Yang, H. Pan, F. Zhang, M. L. Cohen, and S. Zhang, Nano Lett. **15**, 6974 (2015).

[39] J.-T. Wang, H. Weng, S. Nie, Z. Fang, Y. Kawazoe, and C. Chen, Phys. Rev. Lett. **116**, 195501 (2016).

[40] Y. Cheng, J. Du, R. Melnik, Y. Kawazoe, and B. Wen, Carbon **98**, 468 (2016).

[41] M. Ezawa, Phys. Rev. Lett. **116**, 127202 (2016).

[42] M. Hirayama, R. Okugawa, T. Miyake, and S. Murakami, Nat. Commun. **8**, 14022 (2017).

[43] R. Li, H. Ma, X. Cheng, S. Wang, D. Li, Z. Zhang, Y. Li, and X.-Q. Chen, Phys. Rev. Lett. **117**, 096401 (2016).

[44] L.-Y. Gan, R. Wang, Y. Jin, D. Ling, J. Zhao, W. Xu, J. Liu, and H. Xu, Phys. Chem. Chem. Phys. **19**, 7245 (2017).

[45] H. Weng, C. Fang, Z. Fang, and X. Dai, Phys. Rev. B **94**, 165201 (2016).

[46] Z. Zhu, G. W. Winkler, Q. S. Wu, J. Li, and A. A. Soluyanov, Phys. Rev. X **6**, 031003 (2016).

[47] J. L. Lu, W. Luo, X. Y. Li, S. Q. Yang, J. X. Cao, X. G. Gong, and H. J. Xiang, Chin. Phys. Lett. **34**, 057302 (2017).

[48] L. S. Xie, L. M. Schoop, E. M. Seibel, Q. D. Gibson, W. Xie, and R. J. Cava, APL Mater. **3**, 083602 (2015).

[49] C. Fang, M. J. Gilbert, X. Dai, and B. A. Bernevig, Phys. Rev. Lett. **108**, 266802 (2012).

[50] B. J. Wieder, Y. Kim, A. M. Rappe, and C. L. Kane, Phys. Rev. Lett. **116**, 186402 (2016).

[51] S.-M. Huang, S.-Y. Xu, I. Belopolski, C.-C. Lee, G. Chang, T.-R. Chang, B. Wang, N. Alidoust, G. Bian, M. Neupane *et al.*, Proc. Natl. Acad. Sci. USA **113**, 1180 (2016).

[52] B. Bradlyn, J. Cano, Z. Wang, M. G. Vergniory, C. Felser, R. J. Cava, and B. A. Bernevig, Science **353**, aaf5037 (2016).

[53] T.-R. Chang, S.-Y. Xu, D. S. Sanchez, W.-F. Tsai, S.-M. Huang, G. Chang, C.-H. Hsu, G. Bian, I. Belopolski, Z.-M. Yu *et al.*, Phys. Rev. Lett. **119**, 026404 (2017).

[54] A. A. Soluyanov, D. Gresch, Z. Wang, Q. Wu, M. Troyer, X. Dai, and B. A. Bernevig, Nature **527**, 495 (2015).

[55] Z. Wang, D. Gresch, A. A. Soluyanov, W. Xie, S. Kushwaha, X. Dai, M. Troyer, R. J. Cava, and B. A. Bernevig, Phys. Rev. Lett. **117**, 056805 (2016).

[56] K. Deng, G. Wan, P. Deng, K. Zhang, S. Ding, E. Wang, M. Yan, H. Huang, H. Zhang, Z. Xu *et al.*, Nat. Phys. **12**, 1105 (2016).

[57] G. Autès, D. Gresch, M. Troyer, A. A. Soluyanov, and O. V. Yazyev, Phys. Rev. Lett. **117**, 066402 (2016).

[58] M. Kim, C.-Z. Wang, and K.-M. Ho, Phys. Rev. B **96**, 205107 (2017).

[59] M. Yan, H. Huang, K. Zhang, E. Wang, W. Yao, K. Deng, G. Wan, H. Zhang, M. Arita, H. Yang *et al.*, Nat. Commun. **8**, 257 (2017).

[60] H. Huang, S. Zhou, and W. Duan, Phys. Rev. B **94**, 121117 (2016).

[61] K. Zhang, M. Yan, H. Zhang, H. Huang, M. Arita, Z. Sun, W. Duan, Y. Wu, and S. Zhou, Phys. Rev. B **96**, 125102 (2017).

[62] H.-J. Noh, J. Jeong, E.-J. Cho, K. Kim, B. I. Min, and B.-G. Park, Phys. Rev. Lett. **119**, 016401 (2017).

[63] F. Fei, X. Bo, R. Wang, B. Wu, J. Jiang, D. Fu, M. Gao, H. Zheng, Y. Chen, X. Wang *et al.*, Phys. Rev. B **96**, 041201 (2017).

[64] P.-J. Guo, H.-C. Yang, K. Liu, and Z.-Y. Lu, Phys. Rev. B **95**, 155112 (2017).

[65] S. Li, Z.-M. Yu, Y. Liu, S. Guan, S.-S. Wang, X. Zhang, Y. Yao, and S. A. Yang, Phys. Rev. B **96**, 081106 (2017).

[66] T.-R. Chang, I. Pletikosic, T. Kong, G. Bian, A. Huang, J. Denlinger, S. K. Kushwaha, B. Sinkovic, H.-T. Jeng, T. Valla *et al.*, arXiv:1711.09167.

[67] J. He, X. Kong, W. Wang, and S.-P. Kou, New J. Phys. **20**, 053019 (2018).

[68] T. E. O'Brien, M. Diez, and C. W. J. Beenakker, Phys. Rev. Lett. **116**, 236401 (2016).

[69] Z.-M. Yu, Y. Yao, and S. A. Yang, Phys. Rev. Lett. **117**, 077202 (2016).

[70] S. Tchoumakov, M. Civelli, and M. O. Goerbig, Phys. Rev. Lett. **117**, 086402 (2016).

[71] A. Alexandradinata and L. Glazman, Phys. Rev. Lett. **119**, 256601 (2017).

[72] R. Chen, B. Zhou, and D.-H. Xu, Phys. Rev. B **97**, 155152 (2018).

[73] J. P. Perdew and A. Zunger, Phys. Rev. B **23**, 5048 (1981).

[74] A. M. Rappe, K. M. Rabe, E. Kaxiras, and J. D. Joannopoulos, Phys. Rev. B **41**, 1227 (1990).

[75] P. Giannozzi, S. Baroni, N. Bonini, M. Calandra, R. Car, C. Cavazzoni, D. Ceresoli, G. L. Chiarotti, M. Cococcioni, I. Dabo *et al.*, J. Phys.: Condens. Matter **21**, 395502 (2009).

[76] H. J. Monkhorst and J. D. Pack, Phys. Rev. B **13**, 5188 (1976).

[77] M. L. Sancho, J. L. Sancho, and J. Rubio, J. Phys. F **14**, 1205 (1984).

[78] M. L. Sancho, J. L. Sancho, J. L. Sancho, and J. Rubio, J. Phys. F **15**, 851 (1985).

[79] N. Marzari, A. A. Mostofi, J. R. Yates, I. Souza, and D. Vanderbilt, Rev. Mod. Phys. **84**, 1419 (2012).

[80] N. Marzari and D. Vanderbilt, Phys. Rev. B **56**, 12847 (1997).

[81] A. A. Mostofi, J. R. Yates, Y.-S. Lee, I. Souza, D. Vanderbilt, and N. Marzari, Comput. Phys. Commun. **178**, 685 (2008).

[82] I. Souza, N. Marzari, and D. Vanderbilt, Phys. Rev. B **65**, 035109 (2001).

[83] G. Kresse and J. Furthmüller, Phys. Rev. B **54**, 11169 (1996).

[84] J. Heyd, G. E. Scuseria, and M. Ernzerhof, J. Chem. Phys. **118**, 8207 (2003).

[85] See Appendix A for the HSE06 results.

[86] G. V. Vajenine, Solid State Sci. **10**, 450 (2008).

[87] C. Sommer, P. Krüger, and J. Pollmann, Phys. Rev. B **85**, 165119 (2012).

[88] See Table IV in Appendix C for parameter sets for the pristine, 1%, 2%, 3%, 4%, and 5%-strained cases.

[89] S. Ahn, E. J. Mele, and H. Min, Phys. Rev. Lett. **119**, 147402 (2017).

[90] J. P. Carbotte, J. Phys.: Conden. Matter **29**, 045301 (2017).

[91] G. D. Mahan, *Many-particle physics* (Springer Science & Business Media, 2013).

[92] See Table IV (Appendix C) for the $\boldsymbol{k} \cdot \boldsymbol{p}$ parameters used to calculate the optical conductivities.

[93] F. Dieter and J. Martin, Angew. Chem. Int. Ed. **41**, 1755 (2002).

[94] R. Niewa, Angew. Chem. Int. Ed. **41**, 1701 (2002).

[95] G. V. Vajenine, Inorg. Chem. **46**, 5146 (2007).

[96] M. J. Lucero, I. Aguilera, C. V. Diaconu, P. Palacios, P. Wahnón, and G. E. Scuseria, Phys. Rev. B **83**, 205128 (2011).

[97] J. Paier, R. Asahi, A. Nagoya, and G. Kresse, Phys. Rev. B **79**, 115126 (2009).

[98] Y.-S. Kim, M. Marsman, G. Kresse, F. Tran, and P. Blaha, Phys. Rev. B **82**, 205212 (2010).

[99] R. Gillen, S. J. Clark, and J. Robertson, Phys. Rev. B **87**, 125116 (2013).

[100] P. G. Moses, M. Miao, Q. Yan, and C. G. Van de Walle, J. Chem. Phys. **134**, 084703 (2011).